

Getting the manifold right: The crucial role of orbital resolution in DFT+ U for mixed d - f electron compounds

Kinga Warda,^{†,‡,¶,♯} Eric Macke,^{§,||,♯} Iurii Timrov,[⊥] Lucio Colombi Ciacchi,[§] and
Piotr M. Kowalski^{*,†,‡}

[†]*Forschungszentrum Jülich GmbH, Institute of Energy Technologies, Theory and
Computation of Energy Materials (IET-3), Jülich 52425, Germany*

[‡]*Jülich Aachen Research Alliance JARA Energy & Center for Simulation and Data Science
(CSD) 52428 Jülich, Germany*

[¶]*Chair of Theory and Computation of Energy Materials Faculty of Georesources and
Materials Engineering RWTH Aachen University 52062 Aachen, Germany*

[§]*Faculty of Production Engineering, Bremen Center for Computational Materials Science
and MAPEX Center for Materials and Processes, Hybrid Materials Interfaces Group,
University of Bremen, D-28359 Bremen, Germany*

^{||}*U Bremen Excellence Chair, University of Bremen, D-28359 Bremen, Germany*

[⊥]*PSI Center for Scientific Computing, Theory, and Data, 5232 Villigen PSI, Switzerland*

[♯]*Contributed Equally*

E-mail: p.kowalski@fz-juelich.de

Abstract

Accurately modeling compounds with partially filled d and f shells remains a hard challenge for density-functional theory, due to large self-interaction errors stemming from local or semi-local exchange-correlation functionals. Hubbard U corrections can mitigate such errors, but are often detrimental to the description of hybridized states, leading to spurious force contributions and wrong lattice structures. Here, we show that careful disentanglement of localized and delocalized states leads to accurate predictions of electronic states and structural distortions in ternary monouranates (AUO_4 , where A represents Mn, Co, or Ni), for which standard U corrections generally fail. Crucial to achieving such accuracy is a minimization of the mismatch between the spatial extension of the projector functions and the true coordination geometry. This requires Wannier-like alternatives to atomic-orbital projector functions, or corrections of Hubbard manifolds exclusively comprised of the most localized A- $3d$, U- $5f$ and O- $2p$ orbitals. These findings open up the computational prediction of fundamental properties of actinide solids of critical technological importance.

1 Introduction

Computational investigations play a crucial role in the research workflow on energy materials.¹ This is especially the case for nuclear materials, where direct measurements are often limited to surrogate systems in which hazardous actinide elements are replaced by harmless lanthanides.^{2,3} However, the key elements that determine the performance of electrocatalysts, batteries or nuclear fuel and waste, featuring partially filled d and f shells – including transition metals and actinides – pose a challenge for density-functional theory (DFT), the main tool for prediction of the structure and electronic properties of functional materials. This is because the (typically localized) d and f electrons are particularly prone to spurious self-interaction errors (SIEs) that arise from the inexact cancellation of the Hartree term by approximate exchange-correlation (xc) functionals.^{4–6} As a result, several features of exact DFT are not correctly reproduced by LDA and GGA-type xc functionals: the piecewise linearity (PWL) of the total energy with respect to fractional addition or removal of charge,^{4,7,8} the existence of a derivative discontinuity,^{9,10} and the correct asymptotic decay of the Kohn-Sham (KS) potential.¹¹ These shortcomings ultimately compromise the prediction of several fundamental properties, including lattice symmetries, bond strengths and band gaps. For instance, GGA functionals predict UO_2 —the main form of nuclear fuel— to be metallic, whereas it is in fact a Mott insulator with a band gap of ~ 2 eV.¹²

One way to mitigate SIEs is the DFT+ U framework.^{13–16} In this approach, a corrective on-site term scaled by a Hubbard parameter U is applied to a predefined electronic subspace dubbed Hubbard manifold in order to remove (locally) the spurious quadratic deviations from PWL,¹⁷ while also reintroducing a derivative discontinuity. In the commonly used approximation, the Hubbard manifold encompasses the entirety of valence d and f shells, and all magnetic quantum orbitals of these shells are corrected using a *shell-averaged* scalar Hubbard U parameter. This approximation implicitly relies on the assumption that all d and f states are localized and therefore display only weak interactions with the surrounding electron bath. To apply the correction, the orbital occupations within the Hubbard manifold

are determined by projecting the Kohn–Sham wavefunctions onto a suitable mathematical representation, henceforth referred to as Hubbard projectors. A straightforward and widely used choice for this representation consists in atomic-like orbitals parameterized based on solutions of radial Schrödinger equations for isolated atoms. Shell-averaged DFT+ U with such atomic orbital projectors has been successfully applied to study the electronic and ionic structures of a variety of solids bearing lanthanides and actinides.^{18–21}

Geological disposal of nuclear waste is a challenge faced by many countries that utilize nuclear technology.²² A particular concern is the formation of secondary phases between disposed UO_2 -based nuclear fuel, fission products, and near-field elements. A notable example of these secondary phases is provided by ternary monouranates AUO_4 , with A representing a bi- or trivalent metal.²³ Such materials are often studied using DFT+ U schemes. However, for AUO_4 compounds with $\text{A}=\text{Ni}, \text{Mg}, \text{Co}, \text{Mn}$, the shell-averaged approach was shown to incorrectly stabilize a higher-symmetry $Cmmm$ structure instead of the experimentally observed $Ibmm$ phase.²⁴ The failure of shell-averaged DFT+ U was attributed to a significant overestimation of d and f orbital occupancies due to the use of atomic orbital Hubbard projectors, which led to large artificial Hubbard energy contributions.²⁴ To demonstrate this, the authors set the Hubbard energy term E_U to zero, and with this recovered the experimentally observed $Ibmm$ structures. Only for $\text{A}=\text{Cd}$ did the $Cmmm$ structure remain stable, again in line with experimental results. Improvements similar to the $E_U = 0$ procedure were obtained by replacing the atomic-like Hubbard projectors with Wannier-type ones (hereafter denoted as the DFT+ U (WF) method). Wannier-type Hubbard projectors yield more realistic (i.e., closer to integer values) d and f occupations, so that the spurious Hubbard energy contributions vanishes naturally. The DFT+ U (WF) method has also proven valuable in other systems containing actinides and transition-metal (TM) atoms, offering substantial improvements in the predicted electronic structure, thermodynamic properties, and X-ray spectra.^{20,25–28}

Despite these advantages, DFT+ U (WF) comes with practical limitations: the construction of Wannier functions is sensitive to initialization choices (energy windows, number of bands, disentanglement procedure), and — depending on the type of Wannier function used — the direct evaluation of forces and stresses is not yet implemented in the codes. An alternative approach that also seeks to avoid the overcorrections of shell-averaged DFT+ U is orbital-resolved DFT+ U (OR-DFT+ U).²⁹ This method is grounded in the insight that the degree of electron localization (and thus the severity of SIEs) can vary significantly at the *intra-shell* level, i.e., between different nlm orbitals of the same nl subshell.³⁰ OR-DFT+ U provides an *ad-hoc* solution that enables the definition of pinpoint Hubbard manifolds spanned by simple atomic orbital projectors for compounds where shell-averaged DFT+ U fails (Refs. 29,31–34 report examples of such failures).

In this study, we apply various orbital-resolved Hubbard manifolds to the ternary TM monouranates β -NiUO₄, CoUO₄ and MnUO₄, aiming to reproduce the experimentally observed structural distortions without imposing additional constraints on the Hubbard energy or introducing other empirical assumptions or modifications. All Hubbard U parameters are computed from first principles using the linear-response constrained DFT approach (LRC-DFT).^{17,32} By testing different orbital-resolved Hubbard manifolds, we aim at identifying the root cause of the failure of shell-averaged DFT+ U in these systems. Finally, we assess how the definition of the Hubbard manifold and the choice of projector functions influence the prediction of structural observables and clarify under which conditions OR-DFT+ U can serve as a robust and practical alternative to the DFT+ U (WF) framework for modeling d and f electron systems with strong covalent bonding.

2 Materials and methods

2.1 Computational details

DFT calculations were performed using the `pw.x` code contained in the QUANTUM ESPRESSO package.^{35–37} The calculation setup was chosen to match the computational setup used by Murphy et al. This included employing the PBEsol exchange-correlation functional⁹ and ultrasoft pseudopotentials (self-generated using the Vanderbilt code³⁸) with a plane-wave energy cutoff of 50 Ry and a charge density cutoff of 200 Ry. Structural relaxations were carried out until the total energy and atomic forces converged below 10^{-5} Ry and 10^{-4} Ry/Bohr, respectively. All calculations were spin-polarized within the collinear approximation (assuming ferromagnetic order of the TM sites) and used a tight convergence threshold for electronic total-energy self-consistency of 10^{-8} Ry. The projected density of states (PDOS) calculations were performed with a Gaussian broadening of 0.0035 Ry. The option `diag_basis=.true.` in the `projwfc.x` code was enabled to rotate atomic orbitals into the eigenbasis of the occupation matrix, thus aligning orbital projections with the local symmetry and facilitating a clearer identification of orbital character.³⁹

For all DFT+ U calculations¹, we applied the formulation of Dudarev et al. that seeks to mitigate SIEs by enforcing (locally) PWL of the total energy with respect to fractional orbital occupations.^{17,40} We used both shell-averaged and orbital-resolved Hubbard manifolds.^{29,31,32} The OR-DFT+ U energy functional is given by

$$E_{\text{DFT}+U} = E_{\text{DFT}} + E_U, \quad (1)$$

where

$$E_U = \sum_{I,\sigma} \sum_{i=1}^{2l+1} \frac{U_i^I}{2} \lambda_i^{I\sigma} (1 - \lambda_i^{I\sigma}), \quad (2)$$

¹Throughout this work, DFT+ U refers specifically to PBEsol+ U .

and the corresponding Hubbard potential is

$$V_U^\sigma = \sum_I \sum_{i=1}^{2l+1} U_i^I \left(\frac{1}{2} - \lambda_i^{I\sigma} \right) |\phi_i^I\rangle \langle \phi_i^I|. \quad (3)$$

Here, U_i^I is the Hubbard parameter corresponding to the (diagonal) orbital $\{\phi_i^I\}$ of atom I (the principal and angular quantum numbers nl are omitted for clarity), σ is the spin index, and $\lambda_i^{I\sigma}$ are the eigenvalues of the occupation matrix, computed by solving the eigenvalue problem $\sum_{m'} n_{mm'}^{I\sigma} \nu_{m',i}^{I\sigma} = \lambda_i^{I\sigma} \nu_{m,i}^{I\sigma}$, where $\nu^{I\sigma}$ are the corresponding eigenvectors and $n_{mm'}^{I\sigma}$ are the elements of the occupation matrix for the magnetic quantum numbers m and m' . In the shell-averaged case, both expressions simplify as $U_i^I = U^I$ for all i . Orthogonalized atomic orbitals (OAO) $\{\varphi_m^I\}$ were employed as Hubbard projector functions. In Eq. 3, these orbitals are written in their diagonal basis $\{\phi_i^I\}$, which can be back-transformed into the non-diagonal setting by substituting $|\phi_i^{I\sigma}\rangle = \sum_m \nu_{mi}^{I\sigma} |\varphi_m^I\rangle$.²

OAO are closely related to the nonorthogonalized projectors used by Murphy et al., but prevent the double-counting of Hubbard corrections in regions where projector orbitals overlap.^{41,42} With these projector functions, the occupation matrix \mathbf{n} is computed as³

$$n_{mm'}^{I\sigma} = \sum_{\mathbf{k},v} f_{\mathbf{k},v}^\sigma \langle \psi_{\mathbf{k},v}^\sigma | \varphi_{m'}^I \rangle \langle \varphi_m^I | \psi_{\mathbf{k},v}^\sigma \rangle, \quad (4)$$

where m and m' are magnetic quantum numbers, and $\psi_{\mathbf{k},v}^\sigma$ are the KS wavefunctions at point \mathbf{k} with the band index v and spin σ . All on-site U parameters were evaluated from first principles using the LR-cDFT approach introduced in Ref. 17 and extended to the orbital-resolved formalism in Ref. 29. It is important to note that shell-averaged Hubbard U values are not equivalent to the arithmetic mean of the orbital-resolved U parameters associated with a given shell.²⁹ Instead, the shell-averaging is performed at level of the response to the perturbation, which frequently results in shell-averaged U values exceeding both the

²The Hubbard projector functions are independent of spin; however, for each spin channel, they are rotated separately using the corresponding eigenvectors of the spin-resolved occupation matrix.

³Note that additional operators arise when using ultrasoft and PAW basis sets.⁴²

individual orbital-resolved values and their arithmetic mean.³² In the LR-cDFT calculations, perturbations of magnitude $\alpha = \pm 0.05$ eV were applied to the respective manifold of a single atom in a $2 \times 2 \times 2$ supercell that was created to avoid unphysical interactions of the perturbed state with its periodic images. The Brillouin zone was sampled using Γ -centered $4 \times 4 \times 4$ and $2 \times 2 \times 2$ Monkhorst–Pack grids for the unit cell and the supercell calculations, respectively. As the responses to perturbations depend on the electronic structure (which in turn depends on the ionic structure), calculated Hubbard parameters can change when transitioning from a DFT ground state to a DFT+ U one. While there exist procedures that self-consistently derive the Hubbard parameters and optimize the ionic structure,^{43,44} we did not adopt such an approach here. Instead, all LR-cDFT calculations were carried out in a “one-shot” manner on top of DFT+ U ground states obtained using an empirical guess for the U values: $U_{\text{Ni-3d}} = U_{\text{Co-3d}} = 4.0$ eV, $U_{\text{Mn-3d}} = 2.0$ eV, $U_{\text{U-5f}} = 2.0$ eV, and $U_{\text{O-2p}} = 1.0$ eV. This procedure was previously shown to yield Hubbard parameters typically within $\delta U = U_{\text{SC}} - U \leq 0.1$ eV (where U_{SC} is the self-consistent value), provided the input structure does not deviate strongly from the final relaxed one.⁴⁵

2.2 Characterization of the structural distortions

The crystal structure of *Ibmm* ternary monouranates is similar to rutile (TiO_2 , space group $P4_2/mnm$),⁴⁶ featuring parallel one-dimensional chains of edge-sharing AO_6 and UO_6 octahedra that run along the $[001]$ direction (Figure 1a). Each U atom is coordinated by two O1 atoms in a *trans* configuration and four equatorial O2 atoms, whereas the reverse arrangement occurs in the AO_6 octahedra. A distinctive feature of the *Ibmm* structure are strongly hybridized uranyl $\text{O1}=\text{U}=\text{O1}$ moieties, which display significantly shorter bond lengths than the $\text{U}-\text{O2}$ bonds.⁴⁶ These moieties are associated with structural distortions⁴⁷ — namely octahedral tilting (θ , Figure 1b) and off-centering distortions of uranium and oxygen atoms (δ , Figure 1c) — with respect to the higher-symmetry *Cmmm* structure of CdUO_4 . The tilting angle θ measures the deviation of the O2 atoms from collinearity with the b-axis and

is given by

$$\theta = 90^\circ - \tan^{-1} \left[\frac{(2x-1)a}{2zc} \right], \quad (5)$$

where x and z are the fractional coordinates of the O2 atoms, and a and c are lattice parameters. The uranium off-centering δ_U and the oxygen off-centering δ_O are defined as the displacements of the U and O2 atoms from the center of the adjacent AO_6 octahedron, measured along the $[100]$ direction (Figure 1c). Specifically, δ_U and δ_O correspond to the differences between the atomic coordinates of U and O2, and the coordinate of the octahedral center, respectively, all projected onto the $[100]$ direction, capturing the structural distortion along the primary axis of asymmetry. Displacements along other directions are neglected.

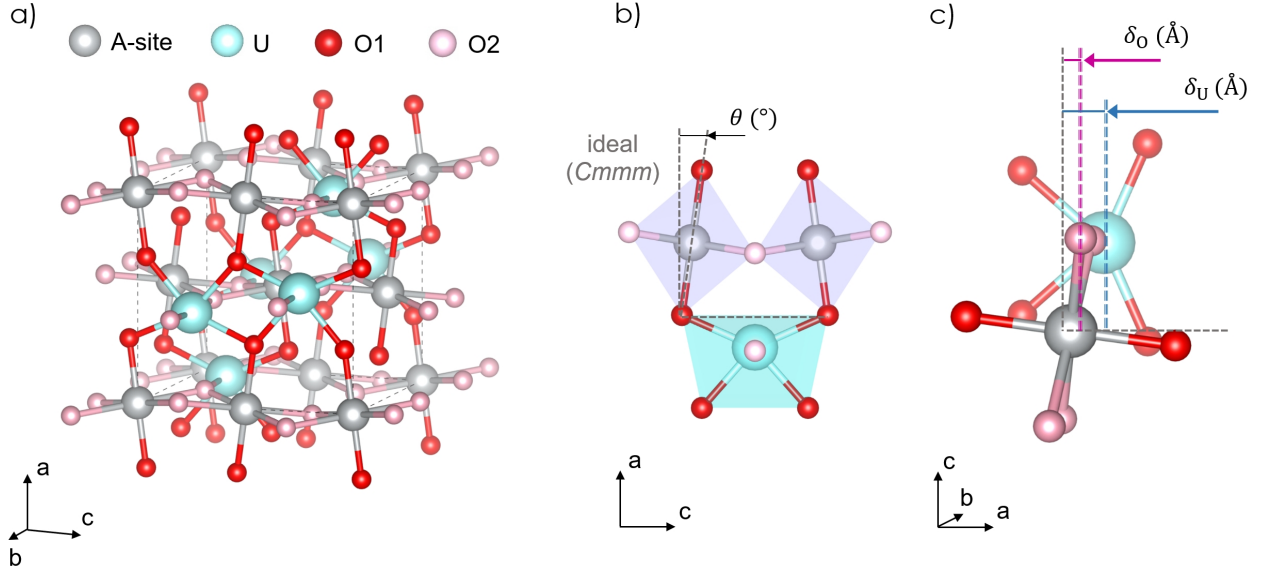


Figure 1: (a) Crystal structure of AUO_4 in the orthorhombic $Ibmm$ space group. Oxygen atoms O1 and O2 are shown in red and pink, respectively. (b) Schematic representation of the AO_6 tilt angle θ around the b -axis, quantifying deviations from the idealized $Cmmm$ symmetry. The UO_6 octahedra is shown in cyan and the AO_6 octahedra in purple. (c) The uranium off-centering δ_U and axial oxygen off-centering δ_O , measured relative to the ideal $Cmmm$ atomic positions. The high-symmetry $Cmmm$ reference structure is indicated by dashed gray lines.

3 Results and discussion

3.1 Response of the structure to variations in U

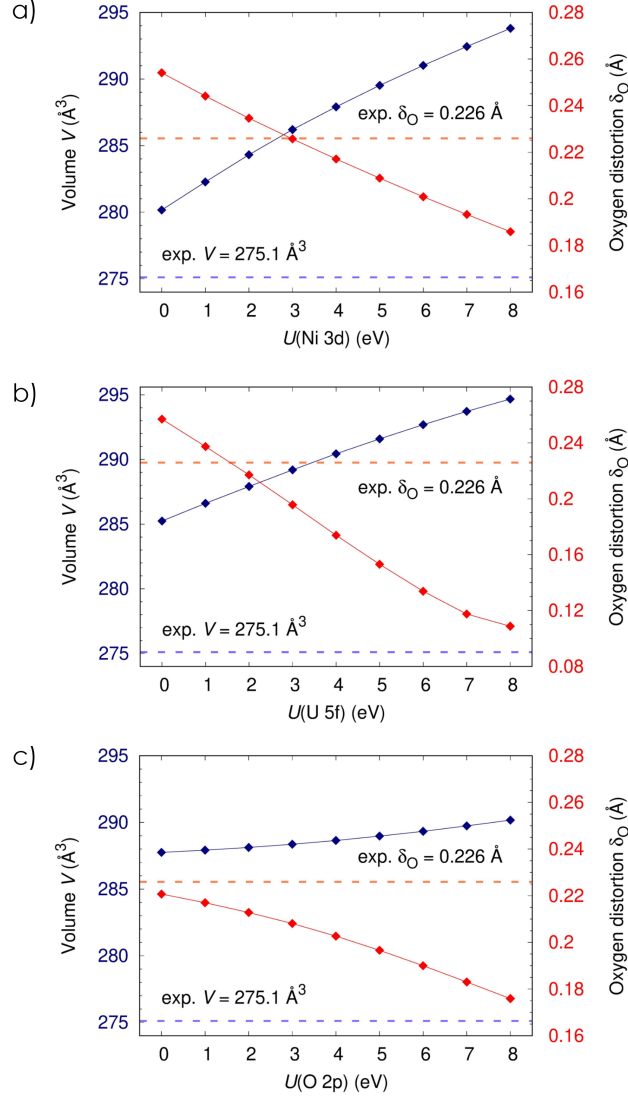


Figure 2: Impact of the Hubbard parameters (a) $U_{\text{Ni-3d}}$ (at fixed $U_{\text{U-5f}} = 2 \text{ eV}$ and $U_{\text{O-2p}} = 1 \text{ eV}$), (b) $U_{\text{U-5f}}$ (at fixed $U_{\text{Ni-3d}} = 4 \text{ eV}$ and $U_{\text{O-2p}} = 1 \text{ eV}$), and (c) $U_{\text{O-2p}}$ (at fixed $U_{\text{Ni-3d}} = 4 \text{ eV}$ and $U_{\text{U-5f}} = 2 \text{ eV}$ fixed) on the cell volume and the magnitude of the oxygen distortion parameter in $\beta\text{-NiUO}_4$. Solid lines serve as a guide for the eye.

To test how AUO_4 structures responds to shell-averaged Hubbard U corrections, we performed geometry optimizations on $\beta\text{-NiUO}_4$ in which the values of $U_{\text{Ni-3d}}$, $U_{\text{U-5f}}$, and $U_{\text{O-2p}}$ were varied systematically. This compound was selected for the analysis because it displays

the most distorted structure. The results, presented in Figure 2, show a strong and monotonic dependence of both the unit cell volume V and the internal distortion parameter δ_O on the applied U values. Specifically, increasing $U_{\text{Ni-}3d}$ from 0 to 8 eV results in a 4.8% expansion of the volume and a 27% reduction in δ_O (Figure 2a). Similarly, increasing $U_{\text{U-}5f}$ from 0 to 8 eV leads to a 3.3% volume expansion and a pronounced reduction in δ_O by 58% (Figure 2b), which reflects the crucial role of the U-5*f* orbitals for the strongly covalent hybridized axial O1=U=O1 bonds. In contrast, applying U corrections to the O-2*p* shell produces a subtler structural response, as increasing $U_{\text{O-}2p}$ from 0 to 8 eV entails only a minimal increase in unit cell volume (0.8%) and a reduction in δ_O by 20% (Figure 2c). The experimental value of δ_O is best reproduced at $U_{\text{Ni-}3d} \approx 3$ eV, $U_{\text{U-}5f} \approx 1.5$ eV and $U_{\text{O-}2p} \approx 0$ eV, whereas the volume is overestimated for all U values, including 0 eV. Qualitatively similar trends are observed for MnUO_4 and CoUO_4 , suggesting that the *Ibmm* structure of AUO_4 compounds manifests a high sensitivity to shell-averaged Hubbard U corrections; at least when the latter are applied through (ortho-)atomic projector functions. For ranges of Hubbard U values that predict correct electronic band gaps (e.g., $U > 6$ eV for Ni-3*d*)⁴⁸ the magnitude of the distortions is severely underestimated, especially since the effects of $U_{\text{Ni-}3d}$, $U_{\text{U-}5f}$, and $U_{\text{O-}2p}$ can be expected to stack (albeit not necessarily in a linear way).

Murphy et al. explained this inconsistent behavior of the U correction with “unrealistic” fractional occupation numbers of unoccupied *d* and *f* orbitals resulting from the use of atomic orbital projectors.²⁴ Due to the functional form of Eq. 2, fractional occupation numbers induce punitive Hubbard energy contributions that grow quadratically with increasing distance from $\lambda = 0$ or $\lambda = 1$ (i.e., E_U is maximized for half-occupied orbitals). Therefore, the minima of the potential energy surface shift towards configurations in which E_U is reduced. For (ortho-)atomic projector functions, this entails the observed volume increase —since larger bond lengths lead to decreased occupations of formally empty orbitals— and causes a linearization of the polyhedral bond angles that reduces the magnitudes of δ_U and δ_O . In Ref. 24 these spurious side-effects of U corrections were mitigated by using WFs as Hubbard pro-

jectors, which yielded occupation numbers much closer to zero or one, or by setting $E_U = 0$ when using atomic Hubbard projectors.²⁴ The fact that the problematic contributions to E_U appear to stem from only a few (formally unoccupied) states raises the question of whether there exists an orbital-resolved Hubbard manifold based on (ortho-)atomic orbital projectors that reduces the sensitivity of the structural parameters to the U values and allows for accurate predictions of the structural distortions without resorting to artificial modifications of the energy functional.

3.2 Determination of orbital-resolved Hubbard manifolds

To identify such orbital-resolved Hubbard manifolds, we analyze the individual orbitals of the A-3d, U-5f and O-2p shells in terms of overlap and occupation patterns. We emphasize that the consideration of O-2p states for the Hubbard manifold is natural because of their potential frontier-state character and high degree of localization.⁴⁹

3.2.1 Group-theoretical analysis of orbital splitting

Before turning to practical calculations, we review the ligand-field-induced splitting of the A-3d and U-5f orbitals from a group theory perspective. In the *Ibmm* crystal structure, the A and U cations occupy the 4a and 4e Wyckoff positions, corresponding to C_{2h} and C_{2v} site symmetries, respectively. The A-3d orbitals transform as two one-dimensional (non-degenerate) irreducible representations: a $3A_g$ representation with contributions from $d_{x^2-y^2}$, d_{z^2} , and d_{xz} , and a $2B_g$ manifold associated with the d_{xy} and d_{yz} atomic orbitals. The lobes of d_{xy} , d_{xz} and d_{z^2} lie between the A–O bond axes and should interact only very weakly with the O-2p orbitals via π overlap (Figure S6). In contrast, the lobes of $d_{x^2-y^2}$ and d_{yz} run along the equatorial and axial A–O bonds, respectively, giving rise to strong σ overlap. Therefore, despite the significant distortions of the AO_6 octahedra, the crystal-field splitting pattern of the A-3d shell can be expected to resemble that of a perfect octahedron with O_h site symmetry. We will thus refer to the three lowest-lying orbitals as $\widetilde{t_{2g}}$, and we designate

the two higher-energy orbitals as $\widetilde{e_g}$, where the tilde denotes the approximate nature of this assignment, since all of the states are non-degenerate in energy.

Moving on, the $5f$ orbitals of U split into seven non-degenerate levels transforming as $2A_1$, $1A_2$, $2B_1$, and $2B_2$. The $1A_2$ representation can be expected to show very little overlap, as the lobes of the corresponding f_{xyz} orbital point away from all bond axes (Figure S6). All other representations are linear combinations of two atomic orbitals and exhibit varying degrees of overlap with adjacent O- sp^2 hybrid orbitals; with the highest energy contributions likely being due to $f_{y(3x^2-y^2)}$ and f_{xz^2} , whose lobes follow the axial O1=U=O1 and the equatorial O2-U-O2 bond axes, respectively (Figure S6).

3.2.2 Analysis of the electronic occupations

Table 1: Eigenvalues λ_i^I corresponding to respective eigenstates ν_i^I in β -NiUO₄, obtained from a DFT+ U calculation with trial Hubbard parameters $U_{\text{Ni-}3d} = 4.0$ eV, $U_{\text{U-}5f} = 2.0$ eV and $U_{\text{O-}2p} = 1.0$ eV.

Atom	Spin	Eigenvalue						
		λ_1	λ_2	λ_3	λ_4	λ_5	λ_6	λ_7
U	\uparrow	0.063	0.107	0.175	0.196	0.247	0.285	0.417
	\downarrow	0.062	0.108	0.150	0.165	0.202	0.241	0.378
Ni	\uparrow	0.972	0.989	0.992	0.994	0.996	-	-
	\downarrow	0.164	0.221	0.983	0.987	0.991	-	-
O ₁	\uparrow	0.748	0.765	0.812	-	-	-	-
	\downarrow	0.736	0.766	0.810	-	-	-	-
O ₂	\uparrow	0.744	0.799	0.802	-	-	-	-
	\downarrow	0.733	0.759	0.799	-	-	-	-

Next, we assess the extent of orbital hybridization by carrying out DFT+ U calculations with shell-averaged trial U values and analyze the resulting electronic structures and orbital occupations. For all trial calculations, we employed $U_{\text{U-}5f} = 2.0$ eV and $U_{\text{O-}2p} = 1.0$ eV. The Hubbard parameters used for the A-site $3d$ shells were system-specific: $U_{\text{Ni-}3d} = 4.0$ eV, $U_{\text{Mn-}3d} = 2.0$ eV, and $U_{\text{Co-}3d} = 4.0$ eV. These comparatively low trial parameters were chosen to avoid analyzing an already overcorrected electronic structure, as spurious effects due to shell-averaged Hubbard U corrections often set in at $U > 4$ eV.^{29,50} The parameter $U_{\text{Mn-}3d}$

was assigned a smaller value than $U_{\text{Ni-3d}}$ and $U_{\text{Co-3d}}$ because previous studies indicate that the Mn-3d shell is often less affected by SIEs than Ni-3d and Co-3d.⁴⁸

The eigenvalues of the occupation matrix, presented in Table 1, clearly reflect the crystal-field splitting between the $\widetilde{e_g}$ and $\widetilde{t_{2g}}$ states of Ni in β -NiUO₄. While eigenstates ν_3 to ν_5 are fully occupied ($\lambda > 0.98$) in both spin channels, λ_1^\downarrow and λ_2^\downarrow are significantly closer to zero (albeit still well above 0.1), indicating formally empty ($\widetilde{e_g}$) states. The remaining eigenstates ν_3^\downarrow to ν_5^\downarrow are again fully occupied, which is consistent with the minority-spin $\widetilde{t_{2g}}$ states of a high-spin d^8 configuration. This assignment is confirmed by the projected density of states (PDOS) shown in Figure 3a, where it can be recognized that the Ni contributions to the conduction bands are exclusively composed of $\widetilde{e_g}$ -like ν_1^\uparrow and ν_2^\downarrow states (Figure 3e). The occupancies of the 3d orbitals of Mn²⁺ and Co²⁺ in MnUO₄ and CoUO₄ show a qualitatively very similar trend (Table S1), and are in line with the expected respective d^5 and d^7 high-spin configurations that were also found by Murphy et al.. In all of the three materials, the 3d shells host formally empty yet significantly occupied $\widetilde{e_g}$ -like eigenstates in the spin-minority manifold that are clearly distinguishable from other empty states by virtue of their elevated eigenvalues ($\lambda > 0.1$), in the PDOS (Figures S1 and S2) and when visualized in real space (Figure S7). These states should not be targeted by on-site Hubbard U corrections, because their fractional occupations are not related to SIEs, but rather stem from the covalent orbital hybridization between metal ions and ligands.^{29,31,51} A reasonable orbital-resolved manifold for the 3d shells therefore consists of the $\widetilde{t_{2g}}$ states, which are relatively localized and exhibit occupation eigenvalues close to either 0 or 1. This target subspace includes ν_3 – ν_5 for β -NiUO₄ (both spin channels), ν_3^\uparrow – ν_5^\uparrow and ν_1^\downarrow – ν_3^\downarrow for MnUO₄, and ν_3^\uparrow – ν_5^\uparrow , ν_1^\downarrow , as well as ν_4^\downarrow – ν_5^\downarrow for CoUO₄. The assignment of the spin-majority eigenstates to either $\widetilde{t_{2g}}$ or $\widetilde{e_g}$ must rely on the eigenvectors, as the corresponding eigenvalues are all close to unity and thus do not allow for a distinction between the two manifolds. Despite their numerical full occupation, the spin-majority $\widetilde{e_g}$ -like eigenstates were also removed from the Hubbard manifold because fully occupied states are still affected by the Hubbard correction via the potential shift of $-U/2$

resulting from Eq. 3. Moreover, an imbalanced correction of spin orbitals (i.e., correcting more spin-majority than spin-minority orbitals) would emulate a Hund J term,^{52,53} which might be useful for addressing fractional spin errors, but a systematic treatment of such effects would go beyond the scope of this study.

For uranium, the PDOS indicates that most $5f$ contributions to the electronic structure are located in the conduction band (Figure 3b); however, the projected occupations of some eigenstates are significantly larger than zero despite the formal $5f^0$ configuration of U^{6+} . Particularly, the high-energy eigenstates ν_5 , ν_6 and ν_7 exhibit eigenvalues above 0.2 (in both spin channels), with λ_7 growing as large as 0.45 in MnUO_4 (Tables 1 and S1). Given the continuous nature of the U- $5f$ occupation spectrum, the definition of an orbital-resolved Hubbard manifold is somewhat ambiguous and cannot be guided by symmetry considerations alone. Based on their comparatively low occupation eigenvalues, we considered the four least-occupied eigenstates (ν_1 – ν_4) to be sufficiently localized to be included in the Hubbard manifold, whereas ν_5 – ν_7 were not targeted by Hubbard corrections to avoid overcorrection due to heavy ligand admixture. To evaluate the robustness of our choice, we examined an alternative definition of the target subspace in which ν_5 was also included. This variation led to only minor changes in the computed values of the U parameters (Table S2).

While partially filled d and f shells are typically the focus of Hubbard U corrections, the possibility that O- $2p$ states might also be localized (and thus require correction of SIEs) is often overlooked. In the present ternary monouranates, the (distorted) trigonal planar coordination geometries of both O sites, with bond angles between 105° and 140° , suggest the presence of three sp^2 hybrid orbitals mediating the interactions between the oxygen atom and the metal centers, and one lone-pair orbital. The sp^2 hybrid orbitals display significant σ -overlap with neighboring A- and U-site cations (for example, Figure 3d shows a σ_{d-p}^* orbital), while the unhybridized p_x/p_y orbitals (depending on whether the site is O1 or O2) interact only slightly with the neighboring sites via π overlap. The occupation eigenvalues of O- $2p$ are far from one, ranging from $\lambda \approx 0.73$ to 0.82 (Table 1 for β - NiUO_4 , Table S2 for

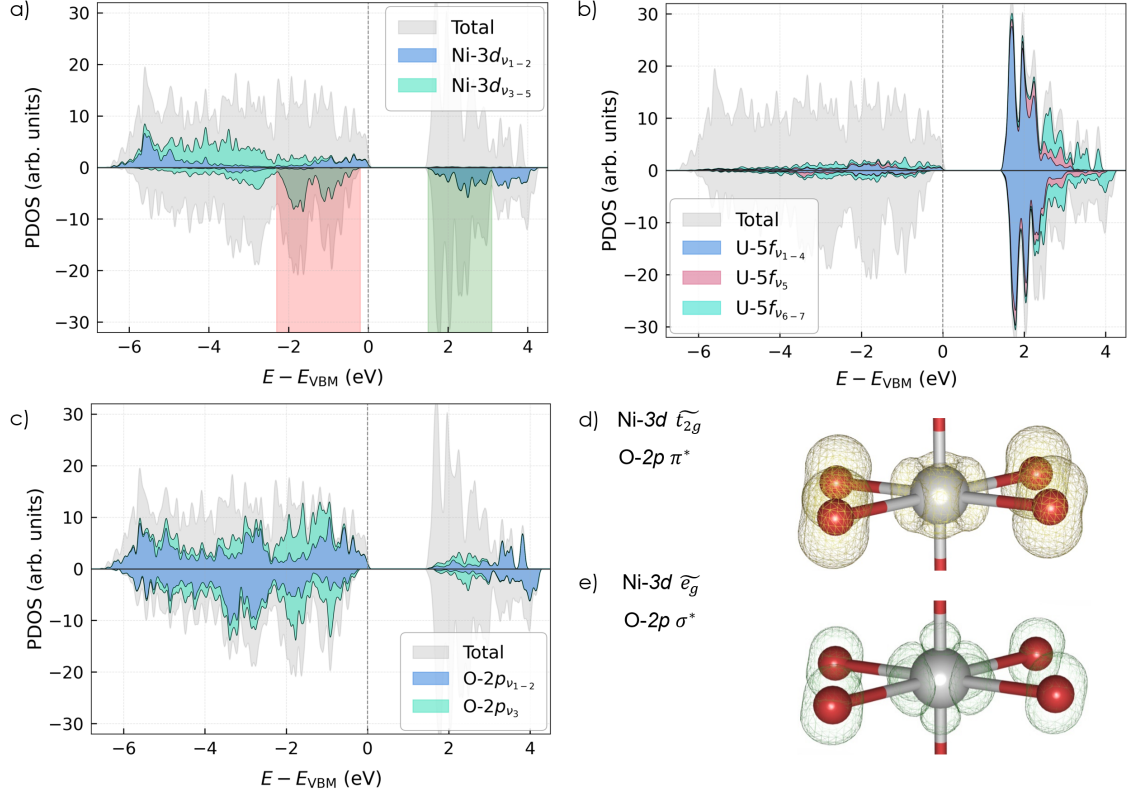


Figure 3: Stacked projected density of states (PDOS) for (a) Ni-3d, (b) U-5f, and (c) O-2p orbitals in β -NiUO₄, obtained from trial DFT+*U* calculations. Panels (d) and (e) show the integrated local density of states for the Ni-3d energy intervals indicated by red and green shading in panel (a) at isovalues $0.0184 \text{ e}^- \cdot \text{\AA}^{-3}$ and $0.0079 \text{ e}^- \cdot \text{\AA}^{-3}$, respectively.

MnUO₄ and CoUO₄). However, there is a noticeable gap between the numerical values of λ_2 (≈ 0.76) and λ_3 (≈ 0.80), except for the spin-up manifold of O2 where both values are similar. Careful analysis of the PDOS shows that energy ranges where $A\text{-}\widetilde{t_{2g}}$ states dominate the electronic structure (e.g., the red shaded area in Figure 3a) also show large contributions due to ν_3 of O-2p. Together with the visualization of the eigenstates (Figure S7), it becomes evident that ν_3 corresponds to the nominally unhybridized p_x (p_y) orbital of O1 (O2). We argue that orbital-resolved Hubbard manifold for O should comprise only this eigenstate, which displays comparatively lower hybridization and a stronger atomic-like character. In contrast, the sp^2 hybridized states are improperly represented by (linear combinations of) 2p OAOs (Figure S7) and show significant delocalization that is not due to SIEs. Hence, ν_1 and ν_2 were not included in the orbital-resolved Hubbard manifold of O-2p, whereas ν_3 was.

3.3 Evaluation of the Hubbard U parameters

Having established orbital-resolved Hubbard manifolds for all frontier shells, we proceed to evaluate the respective Hubbard parameters from LR-cDFT and compare the outcome for different choices of Hubbard manifolds. In the traditional shell-averaged manifold, Hubbard corrections are applied to all A-site $3d$, U- $5f$, and O- $2p$ orbitals. The OR-DFT+ U approach systematically refines this definition of the target subspace through the following sequence of setups with increasingly selective manifolds: (1) The U- $5f$ subspace is restricted to eigenstates $\nu_1-\nu_4$, while shell-averaged U corrections are retained for the A-site $3d$ and O- $2p$ states; (2) as in (1), but with an orbital-resolved U applied to A-site $\widetilde{t_{2g}}$ states; (3) as in (2), but additionally limiting the O- $2p$ correction to the p_x (O1) and p_y (O2) states.

Table 2: Self-consistent Hubbard U parameters obtained from LR-cDFT for four setups (one shell-averaged plus three orbital-resolved) with differently defined Hubbard manifolds. The values in parentheses are those derived and applied by Murphy et al..

System	U (eV)			
Shell-averaged	A- $3d$	U- $5f$	O1- $2p$	O2- $2p$
β -NiUO ₄	7.03 (6.6)	3.65 (2.6)	7.56	7.97
MnUO ₄	7.34 (4.4)	3.92 (2.7)	7.45	7.82
CoUO ₄	6.19 (5.2)	3.77 (2.7)	7.54	7.94
Setup (1)	A- $3d$	U- $5f_{\nu_1-\nu_4}$	O1- $2p$	O2- $2p$
β -NiUO ₄	7.03	1.37	7.59	7.97
MnUO ₄	7.17	1.38	7.49	7.87
CoUO ₄	6.20	1.36	7.56	7.94
Setup (2)	A- $\widetilde{t_{2g}}$	U- $5f_{\nu_1-\nu_4}$	O1- $2p$	O2- $2p$
β -NiUO ₄	7.40	1.33	7.50	7.78
MnUO ₄	1.27	0.93	7.40	7.74
CoUO ₄	2.33	1.22	7.47	7.77
Setup (3)	A- $\widetilde{t_{2g}}$	U- $5f_{\nu_1-\nu_4}$	O1- $2p_x$	O2- $2p_y$
β -NiUO ₄	7.68	1.26	4.14	4.13
MnUO ₄	1.46	1.01	4.25	4.18
CoUO ₄	2.56	1.15	4.11	4.14

Table 2 shows the U values obtained for all choices of Hubbard manifolds and for each compound. While still falling in typical ranges,^{45,49} all shell-averaged U values are comparatively large, and even exceed those reported by Murphy et al. by 1 to 3 eV. The reason for this discrepancy is likely rooted in the use of different Hubbard projector functions: while Murphy et al. employed nonorthogonalized atomic orbitals, here, OAO were used.

Moving forward to setup (1), excluding the most hybridized eigenstates $\nu_5 - \nu_7$ from the Hubbard manifold of U-5*f* prompts a strong and consistent reduction in the corresponding on-site interaction parameters of all three isomorphous compounds, from $U_{\text{U-5}f} \approx 3.8 \text{ eV}$ to $U_{\text{U-5}f_{\nu_1-\nu_4}} \approx 1.4 \text{ eV}$. At the same time, the A-3*d* and O-2*p* manifolds barely respond to the exclusion of $\nu_5 - \nu_7$, maintaining the same U values as in the shell-averaged manifold.

A more drastic drop is observed in setup (2) for MnUO_4 and CoUO_4 , where substituting the shell-averaged $U_{\text{A-3}d}$ correction by a $\widetilde{t_{2g}}$ -specific one leads to U parameters as low as $\approx 1.3 \text{ eV}$ (MnUO_4) and $\approx 2.3 \text{ eV}$ (CoUO_4), respectively. The 1 eV difference between $U_{\text{Mn-}\widetilde{t_{2g}}}$ and $U_{\text{Co-}\widetilde{t_{2g}}}$ can be understood by recognizing that the $\widetilde{t_{2g}}$ subspace of Mn contains three electrons [$\widetilde{t_{2g}}^3(\uparrow)$], whereas that of Co holds five [$\widetilde{t_{2g}}^3(\uparrow)$ and $\widetilde{t_{2g}}^2(\downarrow)$]. In $\beta\text{-NiUO}_4$, however, the $\widetilde{t_{2g}}$ subspace is fully occupied [$\widetilde{t_{2g}}^3(\uparrow)$ and $\widetilde{t_{2g}}^3(\downarrow)$], which causes the manifold to be quite insensitive against perturbations, i.e., its occupations barely change during the course of the LR-cDFT calculations.⁵⁴ This results in a small numerical response that ultimately translates into a large orbital-resolved Hubbard parameter of $U_{\text{Ni-}\widetilde{t_{2g}}} = 7.4 \text{ eV}$. Interestingly, the transition to orbitally-resolved A-3*d* manifolds also affects the U values of the other manifolds, particularly in MnUO_4 , where $U_{\text{U-5}f_{\nu_1-\nu_4}}$ drops by 0.4 eV compared to setup (1), whereas $U_{\text{O1-2}p}$ and $U_{\text{O2-2}p}$ decrease only slightly by $\approx 0.1 \text{ eV}$. This demonstrates the importance of the $\widetilde{e_g}$ states for both intra-shell screening ($\widetilde{t_{2g}} \leftrightarrow \widetilde{e_g}$) and inter-site interactions between the A-3*d* shell and adjacent ligand 2*p* orbitals.

Finally, with setup (3) the U values of oxygen also experience a strong reduction, as the Hubbard U correction to O-2*p* is restricted to the localized p_x (O1) and p_y (O2) orbitals, respectively. Remarkable is not only the drop in values by itself, from ≥ 7.4 down to $\approx 4.2 \text{ eV}$, but also the tightening of the spread (i.e., the difference between the largest and the smallest $U_{\text{O-2}p}$ value), which amounts to $\approx 0.5 \text{ eV}$ in the previous setups but shrinks to only 0.1 eV in setup (3). The fact that $U_{\text{O-2}p_{x/y}}$ is essentially constant, regardless of the A-site cation or the crystallographic site, is a testimony to the almost nonbonding (lone-pair) nature of these orbitals. Nevertheless, with U values on the order of 4.2 eV, they severely contribute

to deviations from PWL; and intriguingly do so much more than the $A-\widetilde{t}_{2g}$ and $U-5f_{\nu_1-\nu_4}$ subspaces.

The strong reduction in U parameters upon transition to orbital-resolved manifolds highlights an important feature of the linear-response formalism, namely that only screening channels outside the target subspace contribute to the effective interaction strength.^{29,53,55} When perturbing entire $5f$, $3d$, or $2p$ shells, important interactions (particularly intra-shell ones like $\widetilde{t}_{2g} \Leftrightarrow \widetilde{e}_g$) are prevented from screening the perturbation, which leads to large U values due to small (apparent) responses. This problem is aggravated by the use of OAO projectors, which often misattribute ligand electrons (e.g., belonging to $O-sp^2$ hybrid orbitals) to metal orbitals, thus even suppressing inter-shell screening pathways. By instead targeting only the most localized frontier orbitals, one mitigates both issues: the relevant intra-shell screening channels remain active, and the misattribution of ligand electrons remains unpunished, as the \widetilde{e}_g and $U-5f_{\nu_5-\nu_7}$ manifolds are not included in the Hubbard manifold. For the AUO_4 systems investigated here, the orbitally-resolved interaction parameters are therefore expected to be more representative of the physical reality than their shell-averaged counterparts.

3.4 Structural distortions

To assess the impact of differently defined Hubbard manifolds on crystal structure predictions, we evaluate the key distortion parameters θ , δ_U and δ_O defined in Sec. 2.2. These distortions are highly sensitive to the underlying electronic structure (and vice versa), illustrated with the PDOSes obtained with different computational schemes in Figures S3–S5 of the SI, and thus provide a meaningful benchmark for this purpose. The PDOSes of the occupied bands obtained with the shell-averaged DFT+ U method [(b) panels] are qualitatively similar to the results of DFT+ U (WF) [(f) panels], with both methods showing pronounced band gap ($\sim 2 - 2.5$ eV). The gradual exclusion of the hybridized states from the Hubbard manifold [(d) and (e) panels] results in a PDOS resembling more closely the DFT results

[(a) panels], with the TM-3d dominated states located close to the valence band maximum. These subtle similarities and differences are taken into account when discussing accuracy of the different methods in predicting the structural distortions.

Figure 4 presents the results for uncorrected DFT (PBEsol), the shell-averaged manifold (shell-averaged DFT+ U) and the three orbital-resolved Hubbard manifolds defined above. For comparison, also shown is the data reported in Ref. 24 for a full-shell manifold applied through WF projectors. Importantly, the projector basis (OAO) is identical for the shell-averaged calculations and the orbitally-resolved ones, so that differences between these approaches arise solely from the specification of the target subspace, rather than from the projectors.

The uncorrected PBEsol functional significantly overestimates the lattice distortions in all three compounds. The most pronounced case is MnUO_4 (Figure 4c/d), where the predicted values of δ_{U} and θ massively exceed the experimental estimates,²⁴ by 241% and 264%, respectively. For $\beta\text{-NiUO}_4$ and CoUO_4 (Figure 4a/b and e/f, respectively), the deviations are slightly less dramatic but remain significant; for instance, θ is off by nearly 90% in CoUO_4 .

If these overestimations stem from SIEs (and the associated spurious over-delocalization of charge), Hubbard U corrections should rectify or at least mitigate them, provided that the Hubbard manifold is defined such that (only) localized frontier states are targeted by the correction.^{10,29} This is seemingly not the case for shell-averaged DFT+ U , which suppresses structural distortions across all compounds. While in $\beta\text{-NiUO}_4$, δ_{U} , δ_{O} , and θ are severely underestimated by up to 500%, MnUO_4 and CoUO_4 are even entirely transformed into the higher-symmetry $Cmmm$ configurations, as all of their distortion parameters fall down to zero (barring numerical noise). The DFT+ U (WF) scheme represents a notable improvement with respect to both uncorrected DFT and shell-averaged DFT+ U , as the Wannier function basis adequately represents frontier orbitals that preserve spatial localization while minimizing overlap with ligand states. With the improved WF Hubbard projectors, the distortion parameters calculated for $\beta\text{-NiUO}_4$ and CoUO_4 are found in good agreement with

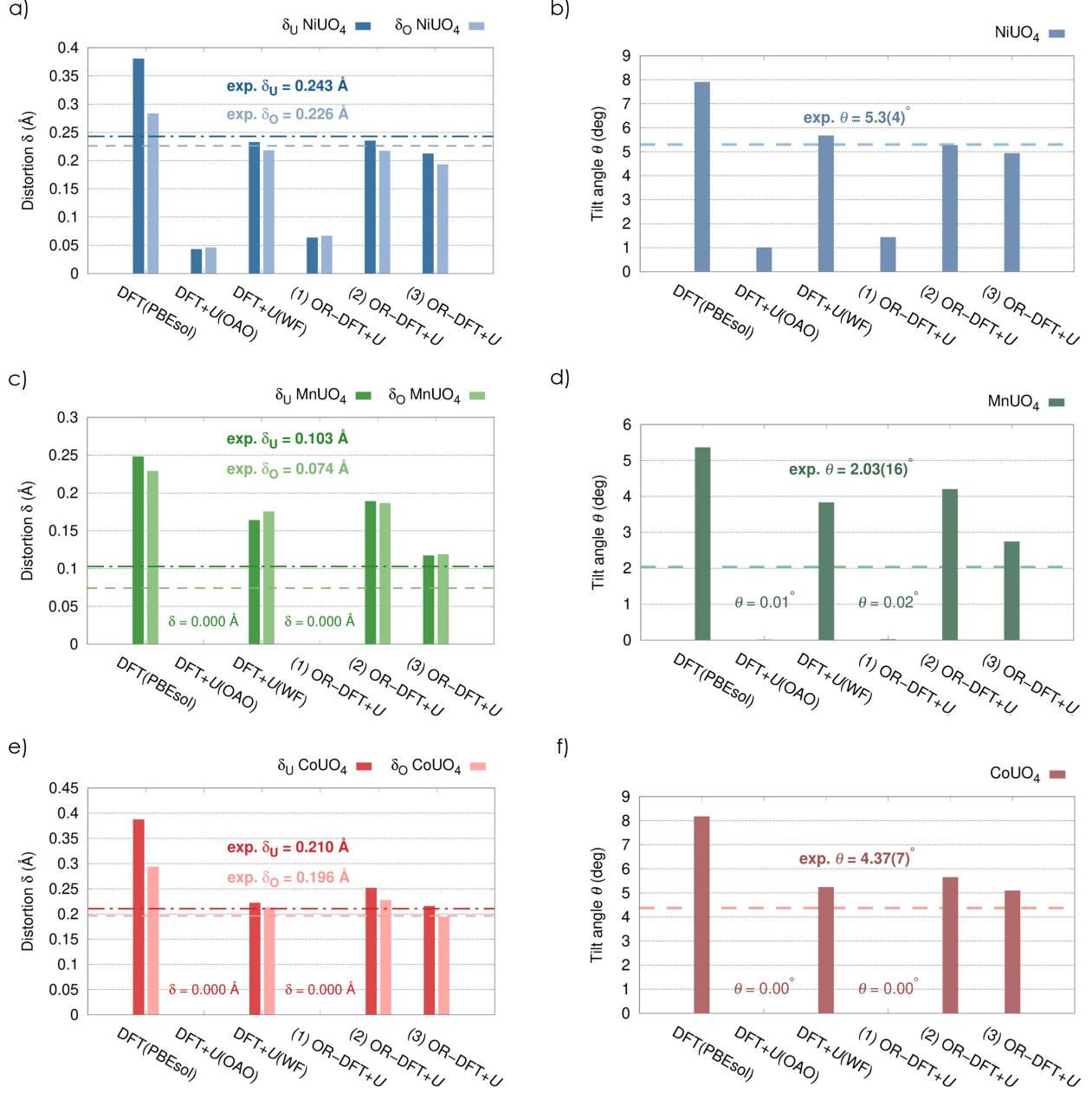


Figure 4: Off-center displacements of uranium, δ_U , and O2 atoms, δ_O (a,c,e), and octahedral tilt angle θ in (b,d,f) as obtained from bare PBEsol and DFT+ U calculations using differently defined Hubbard manifolds (see text and Table 2).

the experiment, deviating by less than 20%. Only for MnUO_4 the accuracy remains less satisfactory, as δ_U , θ and δ_O are overestimated by 59%, 89% and 136%, respectively. The reasons for this inconsistency will be discussed later.

OR-DFT+ U with setup (1) offers no improvement over shell-averaged DFT+ U , as the structural distortions remain suppressed almost entirely across all compounds. This is in spite of the considerable difference between the numerical values of $U_{\text{U-}5f_{\nu_1-\nu_4}}$ and $U_{\text{U-}5f}$. However, the Hubbard corrections to U-5 f mainly affect states in the conduction band, which clearly do not influence the ground-state ionic structures. This result supports previous findings indicating that the symmetry of ternary monouranates is mainly controlled by the A-site cations.^{24,46}

Hence, expanding the orbital resolution to the A-sites' $\widetilde{t_{2g}}$ orbitals within setup (2) markedly improves the accuracy of predictions for β -NiUO₄ and CoUO₄, with δ_{U} , δ_{O} and θ closely matching both experimental values and the results of DFT+ U (WF). However, and similar to DFT+ U (WF), setup (2) still overestimates the distortions in MnUO₄. It is worth noting that Mn²⁺ ions are comparatively large, with an ionic radius of 0.83 Å that exceeds the radii of both Co²⁺ (0.745 Å) and Ni²⁺ (0.69 Å).⁵⁶ Consequently, Mn²⁺ shows a stronger tendency to hybridize with neighboring O-2 p states that is also reflected in the more pronounced variations of the Hubbard U values (Table 2). In view of this, it is no surprise that setup (3), where the Hubbard manifold of O is restricted to the localized p_x/p_y orbitals (in addition to orbitally-resolved corrections to U-5 f and A-3 d), cures the systematic overestimation of distortion parameters in MnUO₄. Fortunately, the orbital-resolved treatment of O-2 p affects the already good predictions of the other two compounds to a much lesser degree: minor improvements result for CoUO₄, where δ_{U} and δ_{O} match the experimental value almost exactly, whereas the accuracy is minimally deteriorated for β -NiUO₄. Therefore, setup (3) provides the most consistent overall accuracy, delivering very good predictions for all distortion parameters and across all compounds. Its dramatic edge over setup (2) and DFT+ U (WF) in MnUO₄ shows the importance of avoiding the correction of strongly hybridized states, here consisting in the bonding σ -states that form between the A- $\widetilde{e_g}$ states and the O- sp^2 hybrid orbitals. More in general, the improvements achieved due to setups (2) and (3) demonstrate that a physically meaningful use of Hubbard U corrections requires

Careful disentanglement of localized and delocalized states. This is particularly crucial for systems where orbital hybridization plays an important role.

3.5 Projector mismatch as a source of spurious Hubbard forces

The profound impact of the Hubbard manifold on the accuracy of structural predictions for AUO_4 compounds demands clarification. While it is generally known that the ionic ground state of $\text{DFT}+U$ can differ significantly from that of the bare functional, it is not understood why and under which circumstances $\text{DFT}+U$ leads to over-symmetrization of atomistic structures, as observed here and reported elsewhere for diverse TM oxides.^{24,50,57–59} In the following, we try to identify the root cause of these deviations and demonstrate why certain Hubbard projector functions or target manifolds perform better than others.

It follows from the Hellmann-Feynmann theorem that the Hubbard energy functional (c.f. Equation 1) contributes an additional term \mathbf{F}_U^I to the total force acting on an ion I :^{42,60}

$$\mathbf{F}_U^I = -\frac{\partial E_U}{\partial \mathbf{R}^I} = -\sum_{\mathbf{k},v,\sigma} \left\langle \psi_{\mathbf{k},v}^\sigma \left| \frac{\partial V_U^\sigma}{\partial \mathbf{R}^I} \right| \psi_{\mathbf{k},v}^\sigma \right\rangle, \quad (6)$$

where \mathbf{R}_I denotes the position of the I th atom. Eq. 6 implies that a finite Hubbard force arises whenever the derivative $\frac{\partial V_U^\sigma}{\partial \mathbf{R}^I}$ is non-zero. Recalling Eq. 3 and assuming a negligible dependence of U on the position, this condition is fulfilled if a displacement of ion I ($\partial \mathbf{R}_I$) modifies the occupation of an eigenstate ($\partial \lambda_i^{I\sigma}$), for instance due to an increase or decrease in its overlap with occupied KS states (in Ref. 61, this is called “density response”).⁴ Because of the form of the Hubbard energy functional, eigenstates with occupation $\lambda_i^{I\sigma} < 0.5$ will experience a force that tends to further reduce their occupation (driving $\lambda_i^{I\sigma} \rightarrow 0$) by lowering their overlap with occupied KS wavefunctions. Conversely, eigenstates with $\lambda_i^{I\sigma} > 0.5$ will tend to increase their occupation. The central question is: why would an eigenstate exhibit

⁴We note that $\frac{\partial V_U^\sigma}{\partial \mathbf{R}^I}$ can also be non-zero if the projectors themselves vary, e.g., due to re-orthogonalization of OAO projectors; these are so-called Pulay forces.⁴²

an occupation far from both zero and one to begin with? This consideration allows us to distinguish two fundamentally different scenarios under which non-zero Hubbard forces arise:

In scenario (i), $\frac{\partial \lambda_i^{I\sigma}}{\partial \mathbf{R}^I} \neq 0$ because the occupation of an eigenstate deviates from zero or one due to violations of the PWL condition. Hence, the resulting forces act to counter the artificial delocalization of states caused by SIEs. In scenario (ii), $\frac{\partial \lambda_i^{I\sigma}}{\partial \mathbf{R}^I} \neq 0$ because the (localized) Hubbard projector functions do not accurately represent the true electron distribution in the system and produce occupation numbers that lie between zero and one, independently of the presence of SIEs. Here, the resulting forces bias the charge density distribution $\rho(\mathbf{r})$ (and therefore also the ionic structure) towards alignment with the Hubbard projector functions. Such forces are artificial and unphysical, since there is no fundamental reason why the electron density of a system should conform to that of an arbitrarily defined set of projector functions. Popular atomic-like projector functions⁵, for example, are constructed based on radial Schrödinger equations for isolated atoms in their neutral charge state. However, the isolated-atom model may not be a reliable approximation for real compounds. This is especially the case for materials with strong covalent bonding (where the quantum numbers n , l and m can lose their physical meaning), for structures with highly distorted bond angles, or when the radius of a charged ion deviates significantly from that of the neutral atom.

Figure 5 illustrates this issue by showing the mismatch between the unoccupied (spin-down) $\widetilde{e_g}$ -like KS orbitals around the Ni^{2+} ion in $\beta\text{-NiUO}_4$ and the diagonal projector orbitals $\phi_{e_g}^\downarrow(\mathbf{r})$ corresponding to eigenstates ν_1^\downarrow and ν_2^\downarrow of the occupation matrix. These eigenstates, which are linear combinations of the OAO projectors (Figures S6 and S7), are indeed fractionally occupied ($\lambda_1^\downarrow \approx 0.16$, $\lambda_2^\downarrow \approx 0.22$, c.f. Table 1). Therefore, applying Hubbard U corrections to this manifold induces an unphysical symmetrization of the structure, as the minimum of this DFT+ U ground state shifts to a configuration where the overlap of the occupied KS states with ν_1 and ν_2 is minimized. Note that such artifacts often remain negligible in highly symmetric systems, including the well-investigated solids FeO and NiO. These

⁵These include NAO, OAO, PAW, and LMTO projectors, among others.

systems exhibit coordination polyhedra with ideal O_h site symmetries, where the angular shape of atomic projectors (e.g., 90° or 180° for d orbitals) coincides with the metal-ligand bond axes.

The observation of an artificial force contribution provides a rationale for the improvements observed when employing either WF projectors or OR Hubbard manifolds. In the former case, it is the projector functions themselves that adapt to the charge density, thus resulting in a less fractional eigenvalue spectrum that yields no spurious force contributions. Conversely, in the latter case, the inadequate eigenstates are simply excluded from the correction by setting $U_i = 0$ for all respective i . Note that spurious Pulay forces due to projector mismatch can also entail “under-symmetrization”, as demonstrated by the improvements in the structural predictions for MnUO_4 upon switching from OR manifold (2) to manifold (3). In manifold (2), the correction targets three sp^2 hybrid orbitals (with bond angles of approximately 120°) plus an unhybridized non-bonding state using three (ortho-)atomic $2p$ projectors (p_x, p_y, p_z). While the non-bonding state (eigenstate ν_3) is well represented by one of the projectors, it is evident that the remaining two projectors (or any linear combination thereof) cannot reproduce the spatial extent of the three sp^2 hybrid orbitals. Consequently,

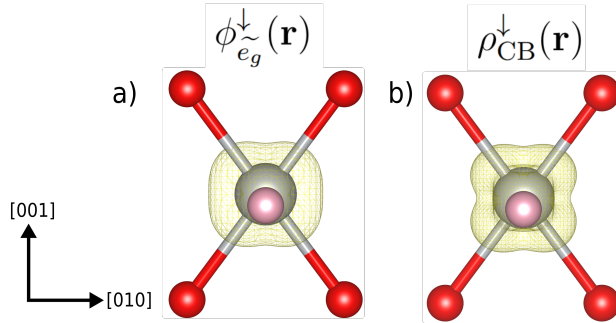


Figure 5: Comparison for $\beta\text{-NiUO}_4$ between the spatial extension of (a) the squared modulus of the Hubbard projector orbitals, $|\phi_{\widetilde{e}_g}^\downarrow(\mathbf{r})|^2 \equiv |\phi_1^\downarrow(\mathbf{r}) + \phi_2^\downarrow(\mathbf{r})|^2 = |\sum_{m=1}^5 (\sum_{i=1}^2 \nu_{mi}^\downarrow) \varphi_m(\mathbf{r})|^2$, representing the formally unoccupied \widetilde{e}_g -like orbitals, and (b) the (pseudo)-charge density due to the KS wavefunctions of the lowest conduction bands in the spin \downarrow channel in the range from 1.8 to 4.2 eV w.r.t. valence band maximum, $\rho_{\text{CB}}^\downarrow(\mathbf{r}) = \sum_{v \in \text{CB}} \sum_{\mathbf{k}} |\psi_{\mathbf{k},v}^\downarrow(\mathbf{r})|^2$ [see Figure 3(a)]. It is the mismatch between projectors and KS wavefunctions that gives rise to the fractional occupation numbers λ_1^\downarrow and λ_2^\downarrow . The color code is the same as in Figure 1.

correcting eigenstates ν_1 and ν_2 of the O-2*p* shell drives the trigonal planar geometry toward an atomic-like one, in which the bond angles are closer to 90°. In the AUO₄ structures considered here, such distortions increase the deviation from the more symmetric *Cmmm* geometry, most significantly in MnUO₄, where interactions between the A-site and neighboring O atoms are strongest due to the relatively large radius of Mn²⁺.

4 Concluding remarks

Using an orbital-resolved DFT+*U* scheme,²⁹ we have demonstrated how the choice of the Hubbard manifold affects the ground-state electronic and structural properties of MnUO₄, CoUO₄ and β -NiUO₄. With (ortho-)atomic projector functions, the characteristic distortions of these monouranates are accurately reproduced only when the Hubbard manifold is restricted to the most localized subset of orbitals within the A-3*d*, U-5*f*, and O-2*p* shells. In contrast, applying Hubbard *U* corrections to more delocalized states within these shells markedly reduces the accuracy. An exception is found for the U-5*f* shell, where the structural distortions are insensitive to the choice of Hubbard manifold, although changes in the electronic structure are still observed (see Figure S4). The generally excessive sensitivity of the ionic structure to the choice of the Hubbard manifold stems from an implicit, artificial contribution in the Hubbard force expression, which aligns the computed charge density $\rho(\mathbf{r})$ (and thus, the ionic positions) with the diagonalized (ortho-)atomic projectors $\phi_i^{I\sigma}(\mathbf{r})$.

Two strategies can help mitigate these artifacts: either one employs Hubbard projector functions that reflect the local bonding environment more faithfully —such as Wannier functions (as practiced in Ref. 24)— or one excludes strongly hybridized states (where the mismatch between $\rho(\mathbf{r})$ and $\phi_i^{I\sigma}(\mathbf{r})$ is large) from the Hubbard manifold using OR-DFT+*U*, as done here. The success of both approaches, DFT+*U*(WF) and OR-DFT+*U*, hinges on an appropriate choice of the Hubbard manifold.⁶ Within the DFT+*U*(WF) framework, this involves the selection of energy windows and sometimes also the disentanglement of

⁶In fact, this applies to all DFT+*U* approaches, including the shell-averaged one.

bands; for OR-DFT+ U with atomic-like Hubbard projectors, one must carefully determine which eigenstates of the occupation matrix exhibit true on-site character, e.g., by analyzing the eigenvalue spectrum. These steps typically require chemical intuition and some degree of trial-and-error, although recent progress on the automation of the Wannierization step^{62,63} has significantly reduced the effort associated with using the DFT+ U (WF) formalism. DFT+ U (WF) might outperform OR-DFT+ U in structures where the mismatch between the true charge density and the shape of atomic-like projectors is extreme, or where Hubbard corrections need to be applied to electronic states localized between atoms (cf. inter-site terms of Refs. 59,64). This can be important when atomic-like projector functions cannot adequately describe a localized manifold, for instance highly localized sp^3 hybrid orbitals. A WF-based approach could still work in such cases because Wannier functions do not make any assumptions regarding the spatial extension of the localized states. On the other hand, owing to its conceptual simplicity, OR-DFT+ U can leverage existing routines for the calculation of forces and stresses, thereby enabling structural relaxations and *ab initio* molecular dynamics, which are often not feasible or not yet available within existing DFT+ U (WF) implementations. Furthermore, due to a more realistic representation of intra-shell screening, OR Hubbard manifolds often acquire lower first-principle U values,²⁹ making the correction even more surgical. Importantly, however, the case of β -NiUO₄ demonstrates that the improvements of OR-DFT+ U with respect to shell-averaged schemes are mainly rooted in the exclusion of hybridized states from the Hubbard manifold, and only to a lesser extent (if any) in the reduction of the U values.

In closing, the results of this work suggest that studying the ground state of structurally complex compounds with distorted polyhedra, mixed valence, and hybridized electronic states requires a chemically informed and orbitally resolved framework, which both OR-DFT+ U and DFT+ U (WF) provide. A priority for future methodological advancements should be the development of nonempirical, quantitative protocols for identifying Hubbard

manifolds (for a given class of projectors) with minimal user input and without reliance on chemical intuition.

Acknowledgement

E.M acknowledges funding by MaX “Materials Design at the Exascale”, a Center of Excellence co-funded by the European High Performance Computing Joint Undertaking (JU) and participating countries under grant agreement No. 101093374. I.T. acknowledges support from the Swiss National Science Foundation (SNSF), grant No. 200021-227641 and No. 200021-236507, and support from the NCCR MARVEL, a National Centre of Competence in Research, funded by SNSF. The authors gratefully acknowledge computing time on the supercomputer JURECA⁶⁵ at Forschungszentrum Jülich under grant No. cjiek61.

Supporting Information Available

Occupation eigenvalues for MnUO_4 and CoUO_4 , projected density of states (PDOS) plots for all Hubbard manifolds and compounds presented, visualization of the OAO projector orbitals and the eigenstates of $\beta\text{-NiUO}_4$, and a detailed description of the tool used to visualize Hubbard projector functions in real space.

References

- (1) Jain, A.; Shin, Y.; Persson, K. A. Computational Predictions of Energy Materials Using Density Functional Theory. *Nat. Rev. Mater.* **2016**, *1*, 15004.
- (2) Chroneos, A.; Rushton, M.; Jiang, C.; Tsoukalas, L. Nuclear Wasteform Materials: Atomistic Simulation Case Studies. *J. Nucl. Mater.* **2013**, *441*, 29–39.

- (3) Bosbach, D.; Brandt, F.; Bukaemskiy, A.; Deissmann, G.; Kegler, P.; Klinkenberg, M.; Kowalski, P. M.; Modolo, G.; Niemeyer, I.; Neumeier, S.; Vinograd, V. Research for the Safe Management of Nuclear Waste at Forschungszentrum Jülich: Materials Chemistry and Solid Solution Aspects. *Adv. Eng. Mater.* **2020**, *22*, 1901417.
- (4) Perdew, J. P.; Zunger, A. Self-Interaction Correction to Density-Functional Approximations for Many-Electron Systems. *Phys. Rev. B* **1981**, *23*, 5048–5079.
- (5) Mori-Sánchez, P.; Cohen, A. J.; Yang, W. Many-electron self-interaction error in approximate density functionals. *J. Chem. Phys.* **2006**, *125*, 201102.
- (6) Kümmel, S.; Kronik, L. Orbital-Dependent Density Functionals: Theory and Applications. *Rev. Mod. Phys.* **2008**, *80*, 3–60.
- (7) Bajaj, A.; Janet, J. P.; Kulik, H. J. Communication: Recovering the flat-plane condition in electronic structure theory at semi-local DFT cost. *J. Chem. Phys.* **2017**, *147*, 191101.
- (8) Burgess, A. C.; Linscott, E.; O’Regan, D. D. DFT+U-type functional derived to explicitly address the flat plane condition. *Phys. Rev. B* **2023**, *107*, L121115.
- (9) Perdew, J. P.; Ruzsinszky, A.; Csonka, G. I.; Vydrov, O. A.; Scuseria, G. E.; Constantin, L. A.; Zhou, X.; Burke, K. Restoring the Density-Gradient Expansion for Exchange in Solids and Surfaces. *Phys. Rev. Lett.* **2008**, *100*, 136406.
- (10) Zhao, Q.; Ioannidis, E. I.; Kulik, H. J. Global and local curvature in density functional theory. *J. Chem. Phys.* **2016**, *145*, 054109.
- (11) Kronik, L.; Kümmel, S. Piecewise Linearity, Freedom from Self-Interaction, and a Coulomb Asymptotic Potential: Three Related yet Inequivalent Properties of the Exact Density Functional. *Phys. Chem. Chem. Phys.* **2020**, *22*, 16467–16481.

- (12) Beridze, G.; Kowalski, P. M. Benchmarking the DFT+ U Method for Thermochemical Calculations of Uranium Molecular Compounds and Solids. *J. Phys. Chem. A* **2014**, *118*, 11797–11810.
- (13) Anisimov, V. I.; Zaanen, J.; Andersen, O. K. Band theory and Mott insulators: Hubbard U instead of Stoner I . *Phys. Rev. B* **1991**, *44*, 943–954.
- (14) Solovyev, I. V.; Dederichs, P. H.; Anisimov, V. I. Corrected atomic limit in the local-density approximation and the electronic structure of d impurities in Rb. *Phys. Rev. B* **1994**, *50*, 16861–16871.
- (15) Liechtenstein, A. I.; Anisimov, V. I.; Zaanen, J. Density-functional theory and strong interactions: Orbital ordering in Mott-Hubbard insulators. *Phys. Rev. B* **1995**, *52*, R5467–R5470.
- (16) Dudarev, S. L.; Botton, G. A.; Savrasov, S. Y.; Humphreys, C. J.; Sutton, A. P. Electron-Energy-Loss Spectra and the Structural Stability of Nickel Oxide: An LSDA+ U Study. *Phys. Rev. B* **1998**, *57*, 1505–1509.
- (17) Cococcioni, M.; De Gironcoli, S. Linear Response Approach to the Calculation of the Effective Interaction Parameters in the LDA+ U Method. *Phys. Rev. B* **2005**, *71*, 035105.
- (18) Chen, J.-L.; Kaltsoyannis, N. DFT+ U Study of Uranium Dioxide and Plutonium Dioxide with Occupation Matrix Control. *J. Phys. Chem. C* **2022**, *126*, 11426–11435.
- (19) Andersson, D. A.; Baldinozzi, G.; Desgranges, L.; Conradson, D. R.; Conradson, S. D. Density Functional Theory Calculations of UO_2 Oxidation: Evolution of UO_{2+x} , U_4O_{9-y} , U_3O_7 , and U_3O_8 . *Inorg. Chem.* **2013**, *52*, 2769–2778.
- (20) Kvashnina, K. O.; Kowalski, P. M.; Butorin, S. M.; Leinders, G.; Pakarinen, J.; Bès, R.; Li, H.; Verwerft, M. Trends in the Valence Band Electronic Structures of Mixed Uranium Oxides. *Chem. Commun.* **2018**, *54*, 9757–9760.

- (21) Blanca Romero, A.; Kowalski, P. M.; Beridze, G.; Schlenz, H.; Bosbach, D. Performance of DFT+U method for prediction of structural and thermodynamic parameters of monazite-type ceramics. *J. Comput. Chem.* **2014**, *35*, 1339–1346.
- (22) Ewing, R. C.; Whittleston, R. A.; Yardley, B. W. Geological Disposal of Nuclear Waste: A Primer. *ELEMENTS* **2016**, *12*, 233–237.
- (23) Murphy, G. L.; Zhang, Z.; Kennedy, B. J. *Complex Oxides*; WORLD SCIENTIFIC, 2019; pp 103–130.
- (24) Murphy, G. L.; Zhang, Z.; Tesch, R.; Kowalski, P. M.; Avdeev, M.; Kuo, E. Y.; Gregg, D. J.; Kegler, P.; Alekseev, E. V.; Kennedy, B. J. Tilting and Distortion in Rutile-Related Mixed Metal Ternary Uranium Oxides: A Structural, Spectroscopic, and Theoretical Investigation. *Inorg. Chem.* **2021**, *60*, 2246–2260.
- (25) Ting, Y.-Y.; Kowalski, P. M. Refined DFT+U Method for Computation of Layered Oxide Cathode Materials. *Electrochim. Acta* **2023**, *443*, 141912.
- (26) He, Z.-D.; Tesch, R.; Eslamibidgoli, M. J.; Eikerling, M. H.; Kowalski, P. M. Low-Spin State of Fe in Fe-doped NiOOH Electrocatalysts. *Nat. Commun.* **2023**, *14*, 3498.
- (27) Vitova, T.; Pidchenko, I.; Biswas, S.; Beridze, G.; Dunne, P. W.; Schild, D.; Wang, Z.; Kowalski, P. M.; Baker, R. J. Dehydration of the Uranyl Peroxide Studtite, $[\text{UO}_2(\eta^2\text{-O}_2)(\text{H}_2\text{O})_2]\cdot 2\text{H}_2\text{O}$, Affords a Drastic Change in the Electronic Structure: A Combined X-ray Spectroscopic and Theoretical Analysis. *Inorg. Chem.* **2018**, *57*, 1735–1743.
- (28) Kowalski, P. M.; He, Z.; Cheong, O. Electrode and Electrolyte Materials From Atomistic Simulations: Properties of Li_xFePO_4 Electrode and Zircon-Based Ionic Conductors. *Front. Energy Res.* **2021**, *9*, 653542.
- (29) Macke, E.; Timrov, I.; Marzari, N.; Ciacchi, L. C. Orbital-Resolved DFT+*U* for Molecules and Solids. *J. Chem. Theory Comput.* **2024**, *20*, 4824–4843.

- (30) Zhou, F.; Ozoliņš, V. Obtaining Correct Orbital Ground States in f -Electron Systems Using a Nonspherical Self-Interaction-Corrected LDA+ U Method. *Phys. Rev. B* **2009**, *80*, 125127.
- (31) Solovyev, I.; Hamada, N.; Terakura, K. T_{2g} versus All $3d$ Localization in LaMO_3 Perovskites ($M=\text{Ti-Cu}$): First-principles Study. *Phys. Rev. B* **1996**, *53*, 7158–7170.
- (32) Pickett, W. E.; Erwin, S. C.; Ethridge, E. C. Reformulation of the LDA + U Method for a Local-Orbital Basis. *Phys. Rev. B* **1998**, *58*, 1201–1209.
- (33) O'Regan, D. D.; Payne, M. C.; Mostofi, A. A. Subspace representations in *ab initio* methods for strongly correlated systems. *Phys. Rev. B* **2011**, *83*, 245124.
- (34) Mariano, L. A.; Vlaisavljevich, B.; Poloni, R. Biased Spin-State Energetics of Fe(II) Molecular Complexes within Density-Functional Theory and the Linear-Response Hubbard U Correction. *J. Chem. Theory Comput.* **2020**, *16*, 6755–6762.
- (35) Giannozzi, P.; Baroni, S.; Bonini, N.; Calandra, M.; Car, R.; Cavazzoni, C.; Ceresoli, D.; Chiarotti, G. L.; Cococcioni, M.; Dabo, I.; Dal Corso, A.; De Gironcoli, S.; Fabris, S.; Fratesi, G.; Gebauer, R.; Gerstmann, U.; Gougoussis, C.; Kokalj, A.; Lazzeri, M.; Martin-Samos, L.; Marzari, N.; Mauri, F.; Mazzarello, R.; Paolini, S.; Pasquarello, A.; Paulatto, L.; Sbraccia, C.; Scandolo, S.; Sclauzero, G.; Seitsonen, A. P.; Smogunov, A.; Umari, P.; Wentzcovitch, R. M. QUANTUM ESPRESSO: A Modular and Open-Source Software Project for Quantum Simulations of Materials. *J. Phys.: Condens. Matter* **2009**, *21*, 395502.
- (36) Giannozzi, P.; Andreussi, O.; Brumme, T.; Bunau, O.; Buongiorno Nardelli, M.; Calandra, M.; Car, R.; Cavazzoni, C.; Ceresoli, D.; Cococcioni, M.; Colonna, N.; Carnimeo, I.; Dal Corso, A.; De Gironcoli, S.; Delugas, P.; DiStasio, R. A.; Ferretti, A.; Floris, A.; Fratesi, G.; Fugallo, G.; Gebauer, R.; Gerstmann, U.; Giustino, F.; Gorni, T.;

- Jia, J.; Kawamura, M.; Ko, H.-Y.; Kokalj, A.; Küçükbenli, E.; Lazzeri, M.; Marsili, M.; Marzari, N.; Mauri, F.; Nguyen, N. L.; Nguyen, H.-V.; Otero-de-la-Roza, A.; Paulatto, L.; Poncé, S.; Rocca, D.; Sabatini, R.; Santra, B.; Schlipf, M.; Seitsonen, A. P.; Smogunov, A.; Timrov, I.; Thonhauser, T.; Umari, P.; Vast, N.; Wu, X.; Baroni, S. Advanced Capabilities for Materials Modelling with Quantum ESPRESSO. *J. Phys.: Condens. Matter* **2017**, *29*, 465901.
- (37) Giannozzi, P.; Barone, O.; Bonfà, P.; Brunato, D.; Car, R.; Carnimeo, I.; Cavazzoni, C.; de Gironcoli, S.; Delugas, P.; Ferrari Ruffino, F.; Ferretti, A.; Marzari, N.; Timrov, I.; Urru, A.; Baroni, S. Quantum ESPRESSO toward the exascale. *J. Chem. Phys.* **2020**, *152*, 154105.
- (38) Vanderbilt, D. Soft Self-Consistent Pseudopotentials in a Generalized Eigenvalue Formalism. *Phys. Rev. B* **1990**, *41*, 7892–7895.
- (39) Mahajan, R.; Timrov, I.; Marzari, N.; Kashyap, A. Importance of Intersite Hubbard Interactions in β -MnO₂: A First-Principles DFT+U+V Study. *Phys. Rev. Mater.* **2021**, *5*, 104402.
- (40) Kulik, H. J.; Cococcioni, M.; Scherlis, D. A.; Marzari, N. Density Functional Theory in Transition-Metal Chemistry: A Self-Consistent Hubbard U Approach. *Phys. Rev. Lett.* **2006**, *97*, 103001.
- (41) Löwdin, P.-O. On the Non-Orthogonality Problem Connected with the Use of Atomic Wave Functions in the Theory of Molecules and Crystals. *J. Chem. Phys.* **1950**, *18*, 365–375.
- (42) Timrov, I.; Aquilante, F.; Binci, L.; Cococcioni, M.; Marzari, N. Pulay Forces in Density-Functional Theory with Extended Hubbard Functionals: From Nonorthogonalized to Orthogonalized Manifolds. *Phys. Rev. B* **2020**, *102*, 235159.

- (43) Cococcioni, M.; Marzari, N. Energetics and Cathode Voltages of LiMPO_4 Olivines (M=Fe,Mn) from Extended Hubbard Functionals. *Phys. Rev. Mater.* **2019**, *3*, 033801.
- (44) Timrov, I.; Marzari, N.; Cococcioni, M. Self-Consistent Hubbard Parameters from Density-Functional Perturbation Theory in the Ultrasoft and Projector-Augmented Wave Formulations. *Phys. Rev. B* **2021**, *103*, 045141.
- (45) Bastonero, L.; Malica, C.; Macke, E.; Bercx, M.; Huber, S. P.; Timrov, I.; Marzari, N. First-Principles Hubbard Parameters with Automated and Reproducible Workflows. *npj Comput. Mater.* **2025**, *11*, 183.
- (46) Baur, W. H.; Joswig, W.; Pieper, G.; Kassner, D. CoReO_4 , a New Rutile-Type Derivative with Ordering of Two Cations. *J. Solid State Chem.* **1992**, *99*, 207–211.
- (47) Murphy, G. L.; Kegler, P.; Zhang, Y.; Zhang, Z.; Alekseev, E. V.; De Jonge, M. D.; Kennedy, B. J. High-Pressure Synthesis, Structural, and Spectroscopic Studies of the Ni–U–O System. *Inorg. Chem.* **2018**, *57*, 13847–13858.
- (48) Uhrin, M.; Zadoks, A.; Binci, L.; Marzari, N.; Timrov, I. Machine Learning Hubbard Parameters with Equivariant Neural Networks. *npj. Comput. Mater.* **2025**, *11*, 19.
- (49) Orhan, O. K.; O’Regan, D. D. First-Principles Hubbard U and Hund’s J Corrected Approximate Density Functional Theory Predicts an Accurate Fundamental Gap in Rutile and Anatase TiO_2 . *Phys. Rev. B* **2020**, *101*.
- (50) Liu, T.-c.; Gaines, D.; Kim, H.; Salgado-Casanova, A.; Torrisi, S. B.; Wolverton, C. Anomalous Reversal of Stability in Mo-containing Oxides: A Difficult Case Exhibiting Sensitivity to DFT+U and Distortion. *Phys. Rev. Mater.* **2025**, *9*.
- (51) Sit, P. H.-L.; Car, R.; Cohen, M. H.; Selloni, A. Simple, Unambiguous Theoretical Approach to Oxidation State Determination via First-Principles Calculations. *Inorg. Chem.* **2011**, *50*, 10259–10267.

- (52) Himmetoglu, B.; Wentzcovitch, R. M.; Cococcioni, M. First-principles study of electronic and structural properties of CuO. *Phys. Rev. B* **2011**, *84*, 115108.
- (53) Linscott, E. B.; Cole, D. J.; Payne, M. C.; O'Regan, D. D. Role of Spin in the Calculation of Hubbard U and Hund's J Parameters from First Principles. *Phys. Rev. B* **2018**, *98*, 235157.
- (54) Kulik, H. J.; Marzari, N. Systematic Study of First-Row Transition-Metal Diatomic Molecules: A Self-Consistent DFT+U Approach. *J. Chem. Phys.* **2010**, *133*, 114103.
- (55) Vaugier, L.; Jiang, H.; Biermann, S. Hubbard U and Hund Exchange J in Transition Metal Oxides: Screening versus Localization Trends from Constrained Random Phase Approximation. *Phys. Rev. B* **2012**, *86*, 165105.
- (56) Shannon, R. D. Revised Effective Ionic Radii and Systematic Studies of Interatomic Distances in Halides and Chalcogenides. *Acta Crystallogr., Sect. A* **1976**, *32*, 751–767.
- (57) Do, H. T.; Lee, A. T.; Park, H.; Ngo, A. T. Delocalized Polaron and Burstein-Moss Shift Induced by Li in α -V₂O₅: A DFT+DMFT Study. *Phys. Rev. B* **2023**, *108*.
- (58) Gebreyesus, G.; Bastonero, L.; Kotiuga, M.; Marzari, N.; Timrov, I. Understanding the Role of Hubbard Corrections in the Rhombohedral Phase of BaTiO₃. *Phys. Rev. B* **2023**, *108*.
- (59) Carta, A.; Timrov, I.; Mlkvik, P.; Hampel, A.; Ederer, C. Explicit Demonstration of the Equivalence between DFT+U and the Hartree-Fock Limit of DFT+DMFT. *Phys. Rev. Res.* **2025**, *7*.
- (60) Himmetoglu, B.; Floris, A.; de Gironcoli, S.; Cococcioni, M. Hubbard-corrected DFT energy functionals: The LDA+U description of correlated systems. *Int. J. Quantum Chem.* **2014**, *114*, 14–49.

- (61) Floris, A.; De Gironcoli, S.; Gross, E. K. U.; Cococcioni, M. Vibrational Properties of MnO and NiO from DFT+U-based Density Functional Perturbation Theory. *Phys. Rev. B* **2011**, *84*.
- (62) Qiao, J.; Pizzi, G.; Marzari, N. Automated Mixing of Maximally Localized Wannier Functions into Target Manifolds. *npj. Comput. Mater.* **2023**, *9*.
- (63) Qiao, J.; Pizzi, G.; Marzari, N. Projectability Disentanglement for Accurate and Automated Electronic-Structure Hamiltonians. *npj. Comput. Mater.* **2023**, *9*.
- (64) Leiria Campo Jr, V.; Cococcioni, M. Extended DFT+ U + V method with on-site and inter-site electronic interactions. *J. Phys.:Condens. Matter* **2010**, *22*, 055602.
- (65) Jülich Supercomputing Centre JURECA: Data Centric and Booster Modules implementing the Modular Supercomputing Architecture at Jülich Supercomputing Centre. *JLSRF* **2021**, *7*.

TOC Graphic

